J Mater Sci (2018) 53:15882–15894

Chemical routes to materials

In-situ construction of 2D direct Z-scheme g-C_3N_4/g-C_3N_4 homojunction with high photocatalytic activity

Qing Qiao[1], Wei-Qing Huang[1,*], Yuan-Yuan Li[1], Bo Li[1], Wangyu Hu[1], Wei Peng[1], Xiaoxing Fan[2], and Gui-Fang Huang[1,*]

[1] Department of Applied Physics, School of Physics and Electronics, Hunan University, Changsha 410082, China
[2] School of Physics, Liaoning University, Shenyang 110036, People's Republic of China

Received: 24 April 2018
Accepted: 30 July 2018
Published online: 3 August 2018

ABSTRACT

Constructing all-solid-state Z-scheme junction is a very effective strategy to design highly active photocatalysts for solar energy conversion and environmental purification. We herein firstly construct 2D g-C_3N_4/g-C_3N_4 Z-scheme homojunction by using a bottom-up approach, during which the supramolecular complex is initially formed, followed by a facile thermal polycondensation. Based on the active species trapping experiments, Mott–Schottky test and band edge position analysis, the prepared 2D nanosheet g-C_3N_4/g-C_3N_4 homojunctions are found to be Z-scheme type, different from those available reported ones with a type-II energy alignment. Benefiting from the specific 2D morphology with large exposed surface area and Z-scheme junction with efficient separation and high redox abilities of the photoinduced electrons and holes, the obtained 2D g-C_3N_4/g-C_3N_4 homojunctions are much more active than the conventional g-C_3N_4/g-C_3N_4 homojunction (CN-MT) and bulk g-C_3N_4 (CN-M) under visible light irradiation, validating by the high rhodamine degradation rate of 0.833 h^{-1}, which is about 3.9 and 15.4 times higher than that of CN-MT (0.214 h^{-1}) and CN-M (0.054 h^{-1}), respectively. The present work sheds light on design of novel Z-scheme photocatalysts with specific morphology and thus further application in the field of environment or energy.

Introduction

Semiconductor-based photocatalysis provides a potentially green and ideal approach in alleviating the shortage of energy and environmental contamination [1–4]. As a representative visible light photocatalyst, graphitic carbon nitride (g-C_3N_4) has attracted considerable attention due to its thermal and chemical stability, non-toxic and low cost. Unfortunately, the photocatalytic performance of pristine g-C_3N_4 prepared by direct pyrolysis of nitrogen rich precursors is far from satisfactory on account of the intrinsic deficiencies, such as insufficient active sites and rapid recombination of photoinduced charge carriers [1]. Therefore, various strategies, such as doping [5], morphology

Address correspondence to E-mail: wqhuang@hnu.edu.cn; gfhuang@hnu.edu.cn

https://doi.org/10.1007/s10853-018-2762-x

controlling [6, 7] and heterojunction construction [8–11], are developed to overcome these deficiencies. Among these, heterojunction construction is generally considered as one of the most promising approaches to enhance the photocatalytic activity by boosting photocarrier separation and transfer. Up to date, various g-C_3N_4-based heterojunctions, such as g-C_3N_4/TiO_2 [12], g-C_3N_4/ZnO [13], g-C_3N_4/carbon [9], g-C_3N_4/CeO_2 [14], g-C_3N_4/$CdWO_4$ [15], g-C_3N_4/CeO_2 [16] and g-C_3N_4/CeO_2/ZnO [17], have been developed by coupling with other semiconductor photocatalysts, carbon nanomaterials, and noble metal nanoparticles, to promote the interfacial charge transfer. Despite the enhancing photocatalytic performance of these g-C_3N_4-based heterojunctions, however, the introduction of these extraneous materials may influence the compatibility, and stability of the resultant heterojunctions owing to the diverse physicochemical properties from g-C_3N_4 [18].

It is noteworthy that the electronic band structure of g-C_3N_4 derived from different nitrogen rich precursors is slightly different and the band gap of g-C_3N_4 reported ranges from 2.4 to 2.8 eV [19–23]. Therefore, homojunction construction by coupling two components of g-C_3N_4 with different band-gap structure provides an alternative way. To date, various g-C_3N_4/g-C_3N_4 homojunctions have been synthesized through the pyrolysis of two different precursors. For instance, g-C_3N_4/sulfur-doped g-C_3N_4 isotype heterojunctions obtained with dicyandiamide and trithiocyanuric acid as raw materials demonstrates efficient charge separation and significant enhancement in photocatalytic activity for hydrogen evolution [24]. The g-C_3N_4/g-C_3N_4 homojunctions from urea and thiourea show enhanced photocatalytic activity for NO removal under visible light irradiation due to the prolonged lifetime of charge carriers driven by the band offsets [25]. It is reported that the intrinsic deficiency of fast charge recombination of pristine g-C_3N_4 can be greatly overcome by the formation of both type I g-C_3N_4/g-C_3N_4 homojunctions obtained from melamine and urea and type-II g-C_3N_4/g-C_3N_4 homojunctions from dicyandiamide and urea, which lead to highly enhanced photocatalytic activity [26]. These reports fully verify the slight differences in the band-gap structure of g-C_3N_4 enable the formation of homojunction at the interface of different components, resulting in enhancement of photocatalytic activity. However, g-C_3N_4/g-C_3N_4 homojunctions obtained using the direct pyrolysis of the mixture of precursors generally result in relatively low surface areas and thus limited photocatalytic activity [27]. Recently, meso-g-C_3N_4/g-C_3N_4 nanosheets laminated homojunctions with high surface area and high visible light photocatalytic activity have been synthesized via template-calcination strategy [8]. However, the tedious post-treatment and hazardous chemicals used for the removal of template largely restrict its practical application.

Generally, the molecular cooperative self-assembly is regarded as an effective bottom-up strategy to fabricate specially shaped micro-/nano-materials since the direction and saturation hydrogen bonding leads the molecules to align in a particular order [28, 29]. The well-known supramolecular precursors emerged as potential materials for the preparing of g-C_3N_4 are melamine–cyanuric acid complex with up to three hydrogen bonds between cyanuric acid and melamine, which may form various morphologies according to the solvent from which it is aligned and precipitated [30]. These results indicate that the molecular self-assembly provides an effective approach for the synthesis of g-C_3N_4 with specific morphologies. Up to date, g-C_3N_4 with different morphologies, such as hollow spheres [31], 3D macroscopic assemblies [32], hollow pancake-like, sheet-like and tube-like morphology [30], hierarchical nanostructures [33], are synthesized; and all of these g-C_3N_4 samples display high photocatalytic activity.

Motivated by the above analysis, herein, 2D g-C_3N_4/g-C_3N_4 homojunctions are prepared by heating the supramolecular precursors formed through the molecular self-assembly among melamine, cyanuric acid and thiourea. The prepared g-C_3N_4/g-C_3N_4 homojunctions show nanosheet morphology with high exposed surface area. Moreover, the active species trapping experiments and band edge position estimation analysis confirm the Z-scheme mechanism, which is beneficial for the effective charge separation in the heterojunction. As a result, the prepared 2D g-C_3N_4/g-C_3N_4 homojunctions exhibit markedly improved photocatalytic activity for the degradation of RhB under visible light irradiation, which is 3.9 times higher than the conventional g-C_3N_4/g-C_3N_4 homojunctions synthesized by the thermal polycondensation of melamine and thiourea as precursors. This work provides a facile and economic approach for the construction of Z-scheme g-C_3N_4/g-C_3N_4 homojunctions with

specific morphology and thus paves the way to their photocatalytic application.

Experiment section

Preparation of g-C_3N_4/g-C_3N_4

Melamine (0.015 mol), cyanuric acid (0.02 mol) and thiourea (0.05 mol) are added in 50 mL of deionized water to form suspension. The suspension is stirred under heating until water completely evaporated to form supermolecule precursors. The supermolecule precursors are milled and heated to 550 °C at a heating rate of 2 °C/min in a muffle furnace for 2 h in air. The obtained g-C_3N_4/g-C_3N_4 homojunctions are designated as CN-MCT. For comparison, the conventional g-C_3N_4/g-C_3N_4 homojunctions are synthesized by calcining the melamine and thiourea of same content under the identical condition and the product is labeled as CN-MT. The g-C_3N_4 nanosheet is prepared from melamine–cyanuric acid complex alone with the same synthesis process and is designated as CN-MC. In addition, 0.02 mol melamine or 0.02 mol thiourea is directly calcined alone under the identical condition and the obtained products is marked as CN-M and CN-T, respectively.

Characterization

The Fourier-transform infrared (FTIR) spectra of the samples are recorded on a Bruker spectrometer. The power X-ray diffraction (XRD) patterns of the products are performed on a Siemens D-5000 Advance X-ray diffractometer using Cu Kα radiation (λ = 0.154 nm). Morphologies of the samples are recorded by an S-4800 field emission scanning electron microscopy (FESEM). The Brunauer–Emmett–Teller (BET) surface area of the samples is determined according to the nitrogen adsorption method with the surface analyzer system (Quadrasorb-evo, Quantachrome). The optical absorption properties of samples are evaluated using a UV–VIS diffuse reflectance spectrophotometer (TU-1901, HITACHI, Tokyo, Japan). The photocurrents and Mott-Schottky measurements are taken on a CHI 660E electrochemical workstation (shanghai Chenhua, China) using a standard three-electrode cell with Pt wire as counter electrode and standard Ag/AgCl in saturated KCl as reference electrode. The working electrode is prepared by dip-coating, i.e., 5 mg samples is mixed with 0.5 mL C_2H_6O and 10 μL nafion solution to form slurry, which is then dip-coated onto a 1 cm × 1 cm FTO glass electrode and dried at 80 °C. 0.5 mol/L Na_2SO_4 solution is used as the electrolyte.

Photocatalytic activity test

A low-power 50 W compact fluorescent lamp equipped with a UV cutoff filter ($\lambda > 400$ nm) is used as the visible light source. The photocatalytic activity of the prepared samples is measured by decolorization of RhB (10 mg/L, 40 mL) under visible light irradiation with 10 mg of the synthesized samples. Prior to visible light irradiation, solutions suspended with the samples are sonicated for 15 min in the dark for guarantying the adsorption–desorption equilibrium of RhB on the surface of the samples. During visible light irradiation, 5 mL suspension liquid is withdrawn every 1 h and immediately centrifuged to remove the particles. Then the photocatalytic activity is tested by analyzing the normalized concentration (C/C_0) variations at the maximum absorption wavelength (554 nm) of UV–Vis spectra of residual RhB with a UV–Vis spectrophotometer at room temperature.

The active species trapping experiments

To investigate the active species generated during photocatalysis, the active species trapping experiments are performed by adding 0.05 mM scavengers including ethyl alcohol (C_2H_6O), isopropyl alcohol (C_3H_8O) and 1,4-benzoquinone ($C_6H_4O_2$) for the holes (h^+), hydroxyl radicals ($^{\cdot}OH$) and superoxide radical ($^{\cdot}O_2^-$), respectively. Specific experimental process is the same to the photocatalytic activity experiment.

Result and discussion

Characterization

The chemical structures of samples are analyzed by FTIR spectroscopy to ascertain the formation of supramolecular precursors and g-C_3N_4/g-C_3N_4 composite. Figure 1a displays the FTIR spectra of precursors. It can be found that the triazine ring

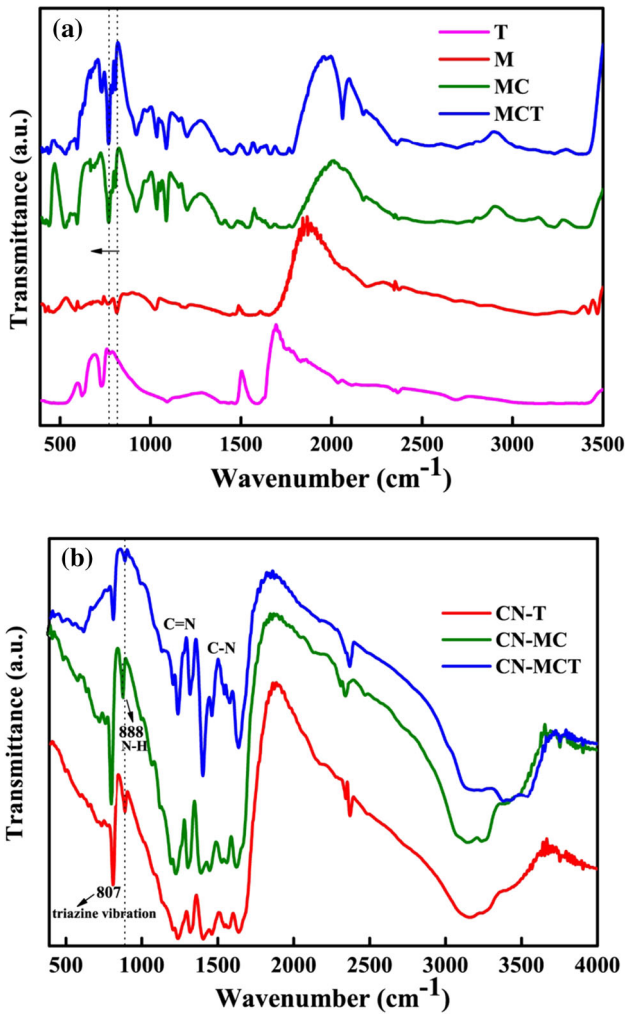

Figure 1 FTIR spectra of **a** T, M, MC and MCT; **b** CN-T, CN-MC and CN-MCT. T: thiourea, M: melamine, MC: supermolecule precursor derives from melamine and cyanuric acid, MCT: supermolecule precursor derives from melamine, cyanuric acid and thiourea. CN-T: g-C_3N_4 derives from thiourea, CN-MC: g-C_3N_4 derives from supermolecule precursor MC, CN-MCT: g-C_3N_4/g-C_3N_4 derives from supermolecule precursor MCT.

vibration of melamine at 816 cm^{-1} shifts to 770 cm^{-1} in the MC and MCT. Furthermore, MC and MCT exhibit several bands between 1300 cm^{-1} and 1600 cm^{-1}, which correspond to the characteristic C–N heterocycles [27]. The variations in the spectra and the appearance of C–N heterocycles confirm the formation of complementary hydrogen bonds between the two components and the successful formation of supermolecule [30, 34]. In order to produce the desired g-C_3N_4 and g-C_3N_4/g-C_3N_4 photocatalyst, the precursors are heated at 550 °C for 2 h and the FTIR spectra of the products are shown in Fig. 1b. It can be observed that the characteristic peaks of melamine disappear, while peaks corresponding to the out of plane breathing vibration characteristic of triazine units appear at about 807 cm^{-1}, and the vibration peaks appeared at ~ 1200, 1237, 1316, 1401, and 1635 cm^{-1} can be assigned to the typical stretching vibration modes of C=N and C–N heterocycles, proving the formation of g-C_3N_4 photocatalyst. The broad band in the range 3000–3600 cm^{-1} is related to secondary and primary amines and their intermolecular hydrogen bonding. And the band at 2377 cm^{-1} can be attributed to the physically adsorptive CO_2 [16, 25]. These results indicate that the products present similar characteristics and retain the basic structure of g-C_3N_4.

The formation of supermolecule precursors and g-C_3N_4/g-C_3N_4 structure are further verified through XRD measurement. As can be observed from Fig. 2a, it is clear that new peaks emerge in MC and MCT compared to that in melamine and thiourea, which suggests new hydrogen-bonding formation between melamine and cyanuric acid and the formation of supermolecule in MC and MCT [30]. The XRD patterns of CN-MT, CN-MC and CN-MCT are displayed in Fig. 2b. All samples show similar XRD patterns that could be ascribed to the typical g-C_3N_4 structure. The two characteristic diffraction peaks at around 2θ = 13° and 27.4° can be indexed to the (100) and (002) planes of g-C_3N_4, respectively, which is in good agreement with previous reports on g-C_3N_4 [35, 36]. Compared with the peaks of CN-MT and CN-MC at 2θ = 27.4°, a minor change is observed with respect to CN-MCT, the (002) peak of CN-MCT shifts to a slight higher angle of 27.7°, which demonstrates the tighter packing aggregates in CN-MCT nanosheets [8, 37, 38].

The morphologies of samples are characterized by SEM images. As can be observed in the SEM images shown in Fig. 3, bulk CN-M and CN-MT display aggregated morphology, consistent with the structure characteristic of g-C_3N_4 prepared by direct polymerization method [38] (Fig. 3a, b). In contrast, the typical morphology of CN-MC and CN-MCT synthesized by calcining the supramolecular precursors appears as nanosheets with a crinkly structure (Fig. 3c, d). The formation of 2D nanosheets is in favor of enhancing the photocatalytic activity in terms of providing high exposed surface area and abundant reactive sites, as well as short diffusion length for decreasing the recombination probability

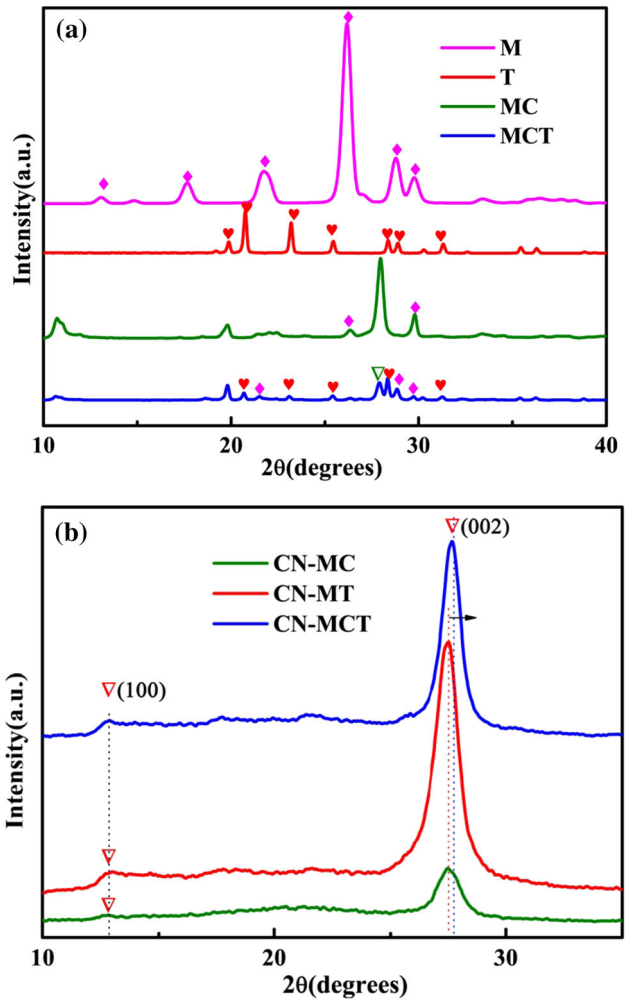

Figure 2 XRD pattern of **a** T, M, MC and MCT; **b** CN-MC, CN-MT and CN-MCT. T: thiourea, M: melamine, MC: supermolecule precursor derives from melamine and cyanuric acid, MCT: supermolecule precursor derives from melamine, cyanuric acid and thiourea. CN-MC: g-C_3N_4 derives from supermolecule precursor MC, CN-MT: the conventional g-C_3N_4/g-C_3N_4 derives from melamine and thiourea, CN-MCT: g-C_3N_4/g-C_3N_4 derives from supermolecule precursor MCT.

of photoinduced charge carriers [39]. It is interesting that 2D g-C_3N_4/g-C_3N_4 homojunctions (Fig. 3d) with intimate interface will further lead to the effective charge transfer. The morphology variation may be related to the intermolecular interaction. According to Figs. 1a and 2a, the specific formation process of ultrathin nanosheets is tentatively illustrated in Fig. 4. As thiourea is added into the suspension of supramolecular aggregates formed through hydrogen bonding between melamine and cyanuric acid, part of the hydrogen bonding between melamine and cyanuric acid will be broken and will form new hydrogen bonding between thiourea and cyanuric acid as illustrated in Fig. 4. Moreover, the gases produced owing to thiourea decomposes during calcination provide a dynamic gas template, facilitating the formation of ultrathin nanosheets [40].

The BET surface areas of CN-T, CN-MC and CN-MCT are evaluated from the adsorption data. The bulk CN-T has the lowest surface area of 17.2 m^2/g, whereas CN-MC and CN-MCT have much larger surface areas of 53.2 m^2/g and 60.9 m^2/g, respectively. The large surface area of CN-MC and CN-MCT can be attributed the preassembled supramolecular precursors, which is beneficial for inhibiting the aggregation of the products and is consistent with the SEM images (Fig. 3).

Optical property

As we all known that the optical absorption of semiconductors is closely related to their electronic structure. The coupling of CN-T with CN-M or CN-MC will greatly affect the optical property of CN-M and CN-MC. In this circumstance, the optical absorption spectra and band structures of the as-prepared samples are analyzed by UV–Vis absorption spectroscopy. As shown in Fig. 5, all samples feature intrinsic semiconductor-like absorption spectra. The CN-M and CN-T exhibit absorption edge at about 470 nm, which can be attributed to the intrinsic band gap of g-C_3N_4, whereas the absorption edge of CN-MC and CN-MCT samples displays an obvious blue shift to around 430 nm and 447 nm, respectively. This phenomenon arises from the well-known quantum confinement effect owing to the formation of ultrathin nanosheets as verified by SEM images. The difference in the energy band gap between CN-T and CN-MC provides the potential for the construction of novel g-C_3N_4-based homojunctions with a well-matched band structure. The absorption edge of CN-MCT is centered at CN-T and CN-MC, and the corresponding energy band gap of CN-MCT (2.76 eV) locates between CN-T (2.58 eV) and CN-MC (2.91 eV) (in the inset of Fig. 5). These results confirm the integration of CN-T and CN-MC in the CN-MCT homojunctions [27].

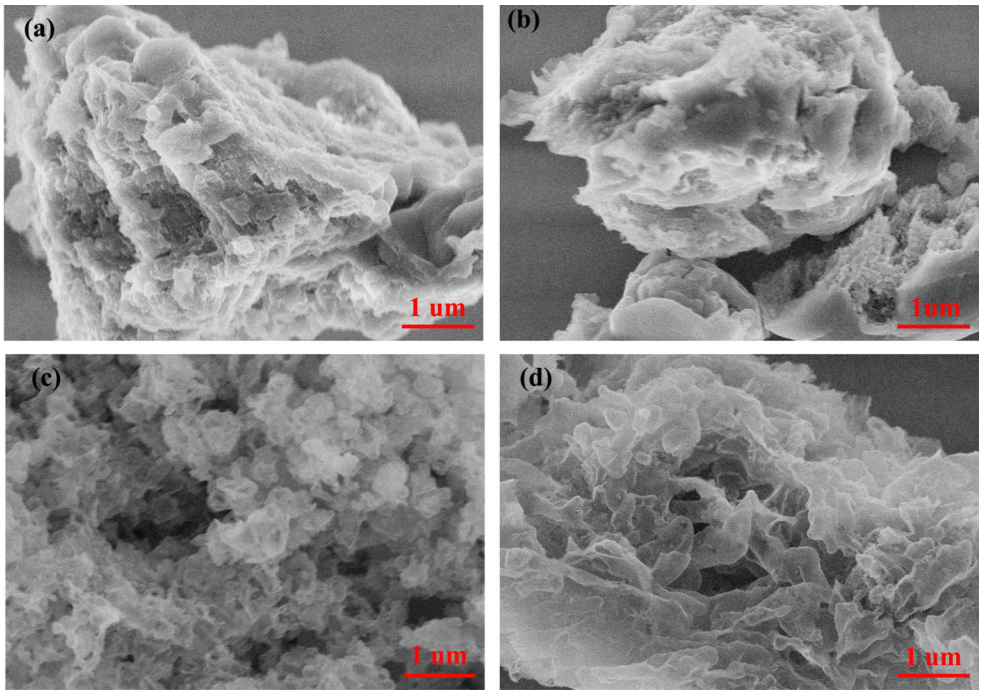

Figure 3 SEM images of **a** CN-M: g-C_3N_4 derives from melamine, **b** CN-MT: the conventional g-C_3N_4/g-C_3N_4 derives from melamine and thiourea, **c** CN-MC: g-C_3N_4 derives from supermolecule precursor MC, **d** CN-MCT: g-C_3N_4/g-C_3N_4 derives from supermolecule precursor MCT.

Photocurrent study

The photocurrent with or without light irradiation is widely used to investigate the separation efficiency of photoinduced charge carriers in the photocatalysts. As shown in Fig. 6, it can be seen that fast photocurrent responses are observed in all the studied electrodes under visible light irradiation. It is worth noting that the photocurrent intensity of CN-MCT homojunction electrode is significantly higher than that of CN-MT and CN-MC, indicting the better interfacial charge transfer and higher efficiency in the separation of photoinduced separation of electron/hole pairs owing to the 2D nanosheet morphology and the formation of the intimate interface in g-C_3N_4/g-C_3N_4 homojunctions.

Photocatalytic performance and stability for RhB degradation

The photocatalytic performance of samples is tested by RhB degradation under visible light irradiation. Relevant experiment results are shown in Fig. 7, the decrease in RhB concentration is negligible in the absence of photocatalyst after 4-h visible light irradiation. It is clear that all the photocatalysts show adsorption capacity; the RhB concentration decreases about 30% in the presence of CN-MCT after reaching adsorption–desorption equilibrium in dark. This adsorption capacity is larger than that obtained with other photocatalysts, which can be attributed to the high exposed surface area of CN-MCT as confirmed by the BET surface area evaluation. The high adsorption capacity of CN-MCT toward RhB molecules is in favor of their photocatalytic degradation. It can be observed from Fig. 7a that the residual RhB can be further decomposed under visible light irradiation. The photocatalytic activity of CN-M and CN-T is relatively low due to the high recombination rate of photoinduced electrons and holes, only about 20% and 30% of RhB is degraded by CN-M and CN-T, respectively, after 4-h visible light irradiation. In contrast, CN-MT and CN-MC exhibit much higher photocatalytic efficiency and about 60% and 88% of RhB is decomposed, respectively, confirming that both the construction of g-C_3N_4/g-C_3N_4 homojunction (CN-MT) from melamine and thiourea and morphology controlling through molecular self-assembly (CN-MC) are the effective strategy to enhance the photocatalytic activity. It is worth noting that RhB is degraded completely after 4-h visible light

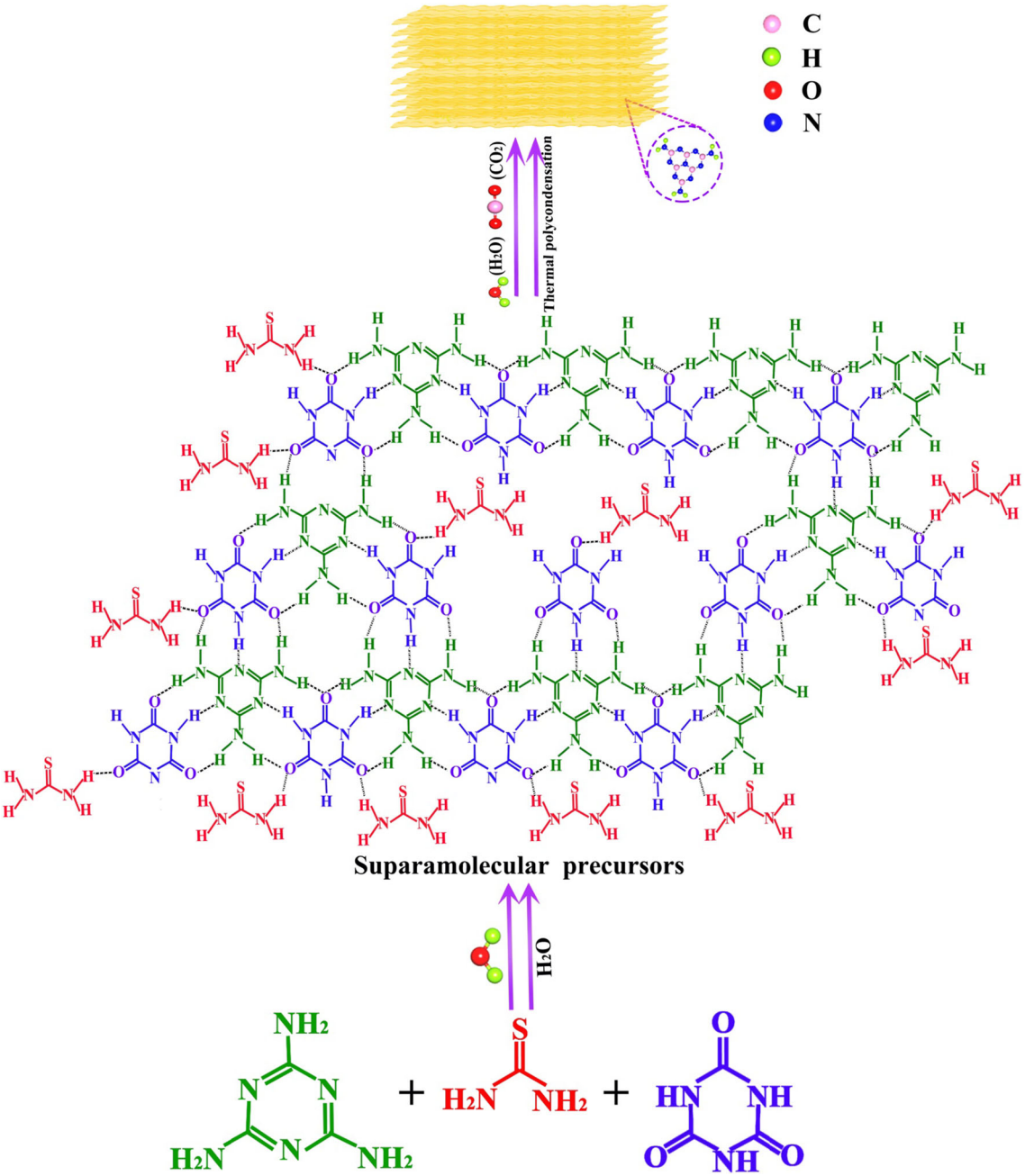

Figure 4 Schematic illustration for the formation of CN-MCT nanosheets. CN-MCT: g-C_3N_4/g-C_3N_4 derives from supermolecule precursor MCT.

irradiation in the presence of CN-MCT, indicating that the synergistic effects of the two strategies greatly improve the overall performance of the photocatalysts and lead to the highest photocatalytic activity owing to the high exposed surface area and improved separation and transfer of photoinduced charges.

To directly compare the photocatalytic activity of samples, the linear relationship of ln (C_t/C_0) versus time is exhibited in Fig. 7b. The rate constant k value is calculated by the following formula.

$$-\ln(C_t/C_0) = kt$$

where C_0 is the equilibrium concentration of RhB after 15 min dark adsorption; C_t is the concentration of RhB after irradiation for t h. The corresponding k values of samples for CN-M, CN-T, CN-MT, CN-MC and CN-MCT are calculated to be 0.054, 0.108,

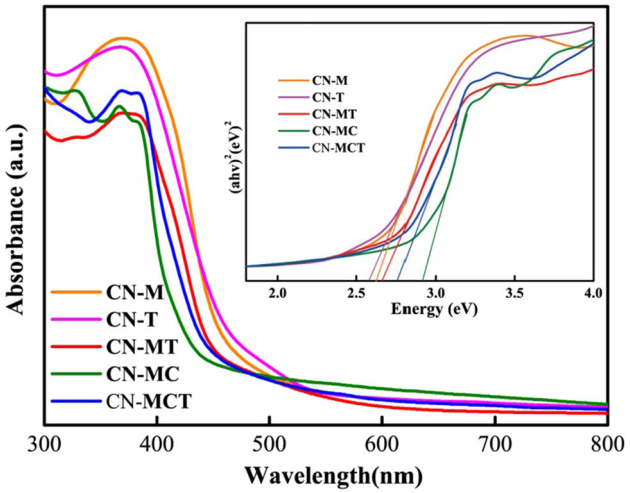

Figure 5 UV-Vis absorption spectra and calculation of the band gap of the CN-M, CN-T, CN-MT, CN-MC, CN-MCT. CN-M: g-C_3N_4 derives from melamine, CN-T: g-C_3N_4 derives from thiourea, CN-MT: the conventional g-C_3N_4/g-C_3N_4 derives from melamine and thiourea, CN-MC: g-C_3N_4 derives from supermolecule precursor MC, CN-MCT: g-C_3N_4/g-C_3N_4 derives from supermolecule precursor MCT.

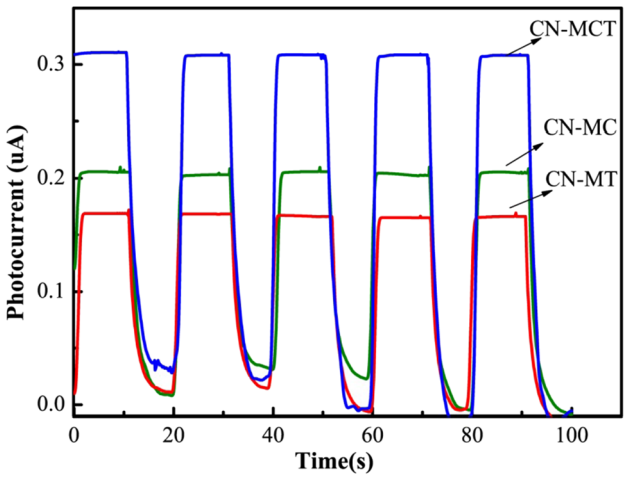

Figure 6 Photocurrent for the CN-MT, CN-MC, CN-MCT electrodes under visible light irradiation ([Na_2SO_4] = 0.5 M). CN-MT: the conventional g-C_3N_4/g-C_3N_4 derives from melamine and thiourea, CN-MC: g-C_3N_4 derives from supermolecule precursor MC, CN-MCT: g-C_3N_4/g-C_3N_4 derives from supermolecule precursor MCT.

0.214, 0.456 and 0.833 h^{-1}, respectively. The rate constant of CN-MCT homojunctions is 1.8, 3.9 and 15.4 times higher than that of CN-MC, CN-MT and CN-M, respectively. These results suggest that the formation of 2D g-C_3N_4/g-C_3N_4 homojunctions through the thermal polycondensation of supramolecular precursors can greatly enhance the

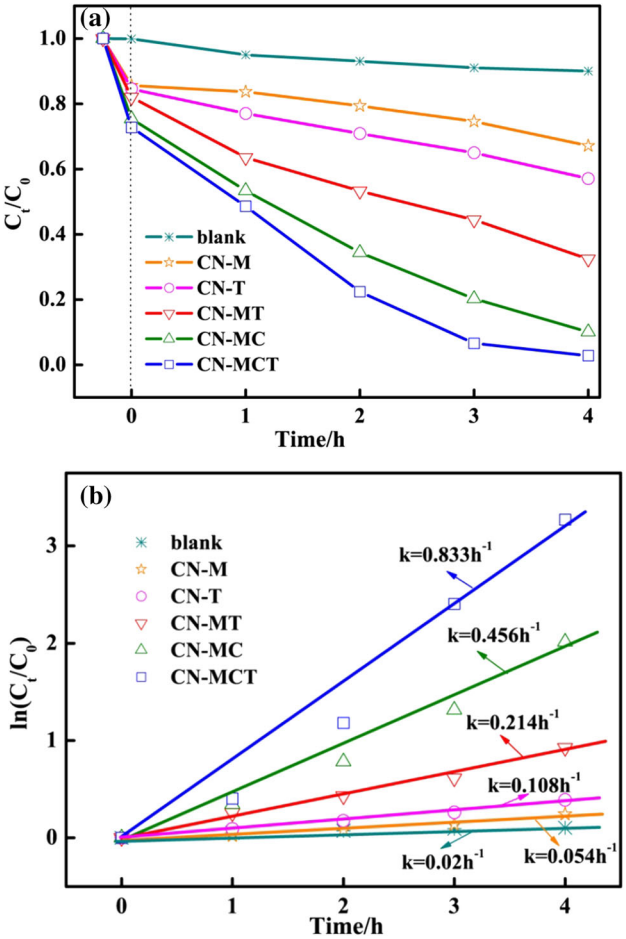

Figure 7 Changes of RhB concentration versus reaction time **a** and the apparent rate constants **b** over the CN-M, CN-T, CN-MT, CN-MC, CN-MCT. CN-M: g-C_3N_4 derives from melamine, CN-T: g-C_3N_4 derives from thiourea, CN-MT: the conventional g-C_3N_4/g-C_3N_4 derives from melamine and thiourea, CN-MC: g-C_3N_4 derives from supermolecule precursor MC, CN-MCT: g-C_3N_4/g-C_3N_4 derives from supermolecule precursor MCT.

photocatalytic performance on the degradation of organic pollutants under visible light irradiation. The 3.9-fold enhancement in the photocatalytic activity of CN-MCT homojunctions compared with the conventional g-C_3N_4/g-C_3N_4 homojunction CN-MT can be attributed to two factors: (1) the more effective charge transfer over 2D g-C_3N_4/g-C_3N_4 homojunctions with intimate interface as illustrated in Fig. 3d and (2) the high surface area and abundant exposed reactive sites provided by the 2D nanosheets. This indicates that the construction of g-C_3N_4/g-C_3N_4 homojunctions through supramolecular approach provides a promising strategy to produce novel morphology and simultaneously optimize the charge transfer process.

Besides the higher photocatalytic activity, the photocatalytic stability and reusability of the photocatalyst is significant for its practical applications. Thus, the stability of photocatalyst CN-MCT is also evaluated by repeating the RhB degradation for four times. It can be observed from Fig. 8 that CN-MCT almost retains its high photocatalytic activity after four times of cycling tests under visible light irradiation, confirming the robust photostability of CN-MCT homojunctions.

Mechanism for the enhanced photocatalytic activity of CN-MCT composites

As is well known, the activity of photocatalyst largely depends on the generation and separation of photoinduced electron–hole pairs, as well as the subsequently produced $\cdot OH$ and $\cdot O_2^-$ radicals, which are usually regarded as the active species in the photocatalytic process. To study the degradation mechanism of RhB, the trapping experiments are applied to identify the main active species during the photocatalytic process in the presence of CN-T, CN-MC and CN-MCT catalyst. As shown in Fig. 9a, the degradation efficiency of RhB over CN-T photocatalyst decreases slightly upon the addition of C_2H_6O and C_3H_8O compared that with no scavengers, suggesting that holes and $\cdot OH$ play minor role in the degradation of RhB under visible light irradiation, whereas the degradation efficiency of RhB decreases significantly, as $C_6H_4O_2$ is added into the reaction

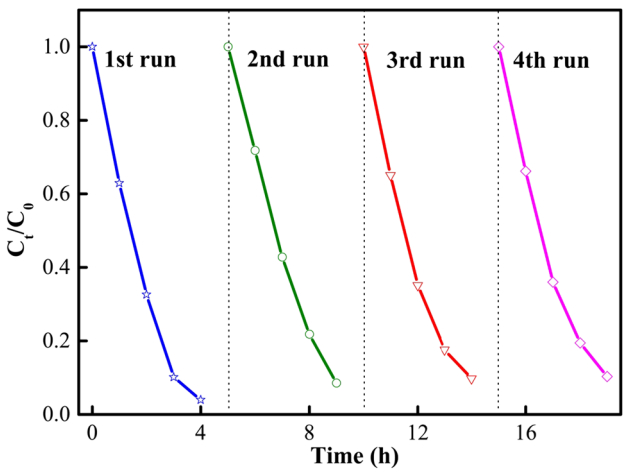

Figure 8 Cycling runs for the photodegradation of RhB in the presence of the CN-MCT under visible light irradiation. CN-MCT: g-C_3N_4/g-C_3N_4 derives from supermolecule precursor MCT.

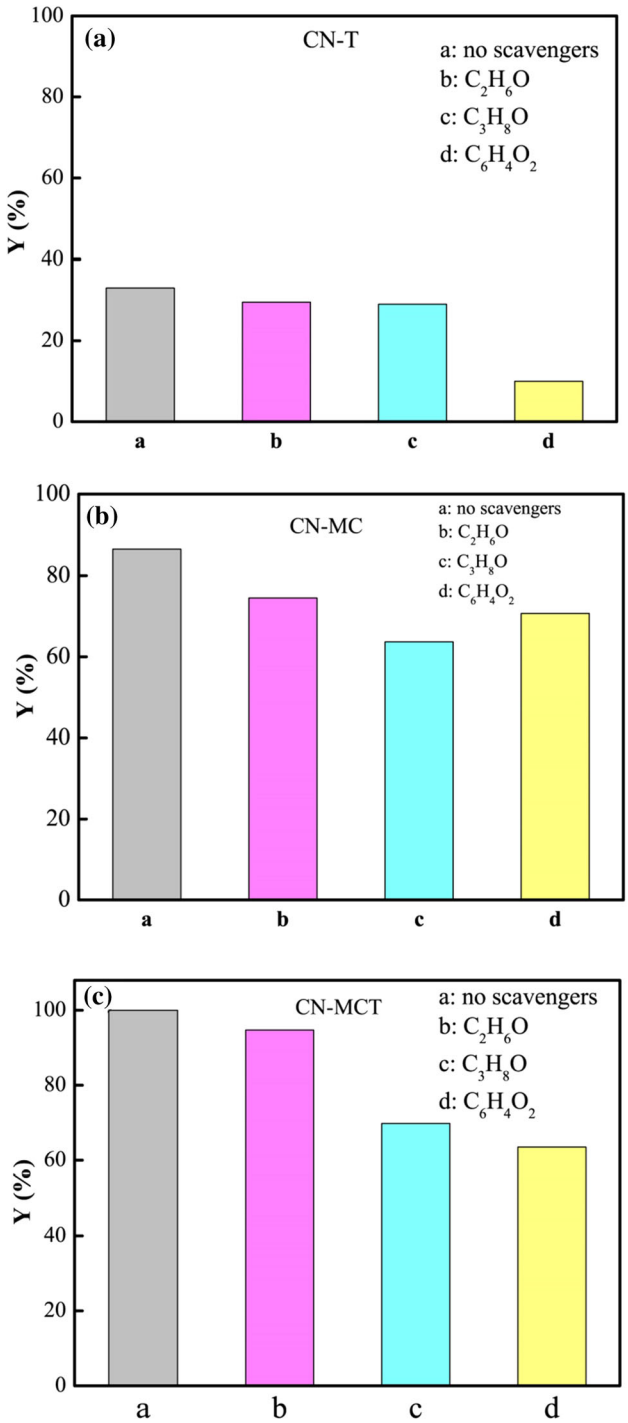

Figure 9 Reactive species trapping experiments over the CN-T, CN-MC and CN-MCT. CN-T: g-C_3N_4 derives from thiourea, CN-MC: g-C_3N_4 derives from supermolecule precursor MC, CN-MCT: g-C_3N_4/g-C_3N_4 derives from supermolecule precursor MCT.

solution for scavenging $\cdot O^{2-}$ radicals, indicating that $\cdot O^{2-}$ are the main active species for RhB photodegradation in the presence of CN-T photocatalyst. While in the presence of CN-MC photocatalyst, the degradation efficiency of RhB shows slight decline as C_2H_6O and $C_6H_4O_2$ is added, but decreases greatly as C_3H_8O is added (Fig. 9b), indicating that the $\cdot OH$ are the main active species for CN-MC photocatalyst. It is worth noting that the degradation efficiency of RhB displays obvious decrease as C_3H_8O or $C_6H_4O_2$ is added in the presence of CN-MCT photocatalyst (Fig. 9c), implying that $\cdot OH$ and $\cdot O^{2-}$ are the main active species in the case of CN-MCT photocatalyst.

To estimate the band positions of photocatalyst and further confirm the photocatalytic mechanism of CN-MCT, electrochemical Mott–Schottky test is performed to evaluate the band positions of photocatalyst. The positive slopes of Mott–Schottky results as shown in Fig. 10 suggest that all the samples are typical n-type semiconductors. The flat potentials as represented by the x intercept of the linear region for CN-T, CN-MC and CN-MCT are estimated to be − 1.35, − 1.3 and − 1.26 V (vs. Ag/AgCl), which corresponds to − 0.74 V, − 0.69 V and − 0.65 V (vs NHE), respectively. As is widely accepted, the flat potential of n-type semiconductor is lower 0–0.1 eV than that of the CB potentials; therefore, the CB potential of CN-T, CN-MC and CN-MCT are − 0.79, − 0.74 and − 0.7 eV, respectively, as the difference is set as 0.05 eV. According to the CB potential and the band-gap values extrapolated by UV–Vis spectra as shown in Fig. 5, the VB potentials are estimated to be 1.79 eV, 2.17 eV and 2.07 eV for CN-T, CN-MC and CN-MCT.

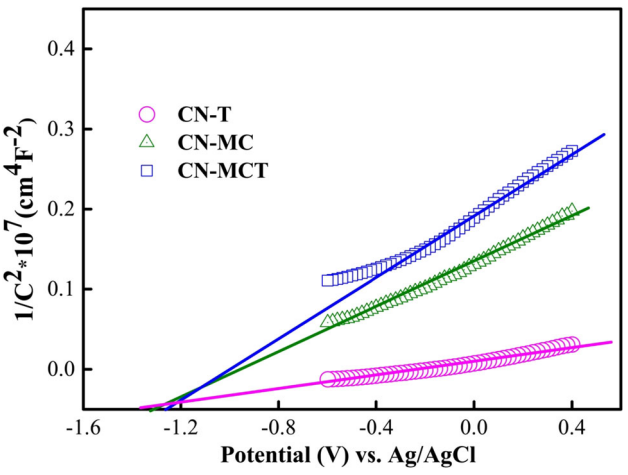

Figure 10 Mott–Schottky plots for the CN-T, CN-MC and CN-MCT. CN-T: g-C_3N_4 derives from thiourea, CN-MC: g-C_3N_4 derives from supermolecule precursor MC, CN-MCT: g-C_3N_4/g-C_3N_4 derives from supermolecule precursor MCT.

On the basis of the above experimental results and discussion, the enhanced photocatalytic activity for RhB degradation over CN-MCT is proposed. CN-MCT displays 2D nanosheets with a crinkly structure, which is different from the aggregated morphology of bulk g-C_3N_4 (Fig. 3), Moreover, CN-MCT has much higher specific surface area (60.9 m^2/g) according to the nitrogen adsorption data and thus provides more active sites for pollutant adsorption and the reaction process. Under visible light irradiation, both CN-T and CN-MC will be excited and photoinduced electrons and holes will be produced on their CB and VB, respectively. In the case of pure CN-T, the photoinduced holes in the VB of CN-T cannot react with the OH^- to generate $\cdot OH$ radicals owing to their weak oxidation ability with negative VB potential of CN-T than that of $OH^-/\cdot OH$ (1.99 eV vs. NHE), while the photoinduced electrons in the CB of CN-T will react with adsorbed oxygen to form $\cdot O^{2-}$ radicals, which act as the main reactive species in the RhB degradation process. While in the case of CN-MC, the photoinduced holes in the VB of CN-MC may directly oxidize the RhB molecules or react with the OH^- to produce •OH radicals, which act as the main reactive species; meanwhile, the photoinduced electrons in the CB of CN-MC can react with adsorbed oxygen to from $\cdot O^{2-}$ radicals, which also take part in the RhB degradation process. For the CN-MCT homojunction with staggered band structure, two transfer pathways of photoinduced charges, traditional type-II heterojunction and Z-scheme system [41], are generally proposed. If the photoinduced charge transfers follow the traditional type-II mechanism, the photoinduced electrons will be injected from the CB of CN-T to CB of CN-MC while the holes will transfer from the VB of CN-MC to VB of CN-T. In this case, the accumulated holes in the VB of CN-T cannot react with the OH^- to generate $\cdot OH$ radicals owing to the negative VB potential of CN-T than that of $OH^-/\cdot OH$ (1.99 eV vs. NHE). So the photoinduced holes will directly participate in the redox reaction and play a major role in the photocatalytic system. This is opposed to the above-mentioned trapping experiments. Therefore, direct Z-scheme system may be formed on CN-MCT heterojunction as shown in Fig. 11. The photoinduced electrons in CB of CN-MC transfer to the VB of CN-T and directly recombine

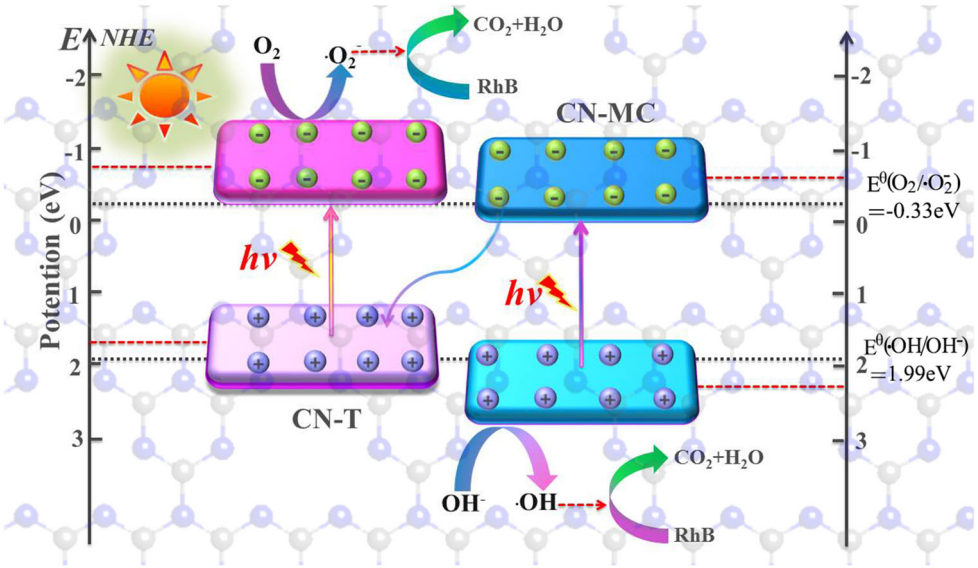

Figure 11 Proposed mechanism for the enhanced photocatalytic activity of the CN-MCT. CN-MCT: g-C_3N_4/g-C_3N_4 derives from supermolecule precursor MCT.

with the photoinduced holes there. As a result, the leaving behind electrons would be accumulated in the CB of CN-T whiles the holes in the VB of CN-MC, respectively. Such spatial separation of the photoinduced electrons and holes greatly inhibits the recombination of electrons and holes. Moreover, the leaving behind electrons and holes with high redox ability will further react with adsorbed oxygen to form $\cdot O^{2-}$ radicals and OH^-/H_2O to generate •OH radicals, respectively. These $\cdot O^{2-}$ and •OH radicals will act as the main active oxygen species for oxidation of organic pollutants. The above trapping experiment result (Fig. 9) further confirms the correctness of Z-scheme photocatalytic mechanism over CN-MCT heterojunction. Therefore, the 2D nanosheets with high exposed surface area and the Z-scheme photocatalytic mechanism with efficient spatial separation and higher redox ability of photoinduced charge carriers lead to the enhanced photocatalytic activity over CN-MCT.

Conclusion

2D g-C_3N_4/g-C_3N_4 homojunction photocatalysts have been successfully prepared through facile calcination of supramolecular complex which are formed through the molecular self-assembly among melamine, cyanuric acid and thiourea. The unique 2D nanosheets provide high exposed surface area. Moreover, the Z-scheme heterojunction of g-C_3N_4/g-C_3N_4 possesses efficient spatial separation and higher redox ability of photoinduced charge carriers. As a result, the obtained CN-MCT homojunction composites show superior photodegradation efficiency of RhB under visible light, and the high RhB degradation rate of 0.833 h^{-1} is about 3.9 and 15.4 times higher than that of the conventional homojunction CN-MT and bulk CN-M, respectively. The supramolecular aggregation provides an effective and promising route for the rational design of active g-C_3N_4-based Z-scheme photocatalysts with specific structure.

Acknowledgements

The authors are grateful to the National Natural Science Foundation of China (Nos. 51772085, 21773099, 51471068 and U1530151), the Aid Program for Science and Technology Innovative Research Team in Higher Educational Institutions of Hunan Province.

References

[1] Ong W-J, Tan L-L, Ng YH et al (2016) Graphitic carbon nitride (g-C_3N_4)-based photocatalysts for artificial photosynthesis and environmental remediation: are we a step closer to achieving sustainability? Chem Rev 116:7159–7329

[2] Schultz DM, Yoon TP (2014) Solar synthesis: prospects in visible light photocatalysis. Science 343:1239176

[3] Xiao J-H, Huang W-Q, Y-s Hu et al (2018) Facile in situ synthesis of wurtzite ZnS/ZnO core/shell heterostructure with highly efficient visible-light photocatalytic activity and photostability. J Phys D Appl Phys 51:075501

[4] You M, Pan J, Chi C et al (2018) The visible light hydrogen production of the Z-scheme Ag_3PO_4/Ag/g-C_3N_4 nanosheets composites. J Mater Sci 53:1978–1986

[5] Feng L-L, Zou Y-C, Li C-G et al (2014) Nanoporous sulfur-doped graphitic carbon nitride microrods: a durable catalyst for visible-light-driven H_2 evolution. Int J Hydrogen Energy 39:15373–15379

[6] Zou L-R, Huang G-F, Li D-F et al (2016) A facile and rapid route for synthesis of g-C_3N_4 nanosheets with high adsorption capacity and photocatalytic activity. RSC Adv 6:86688–86694

[7] Liu C, Huang H, Ye L et al (2017) Intermediate-mediated strategy to horn-like hollow mesoporous ultrathin g-C_3N_4 tube with spatial anisotropic charge separation for superior photocatalytic H_{-2} evolution. Nano Energy 41:738–748

[8] Tan S, Xing Z, Zhang J et al (2017) Meso-g-C_3N_4/g-C_3N_4 nanosheets laminated homojunctions as efficient visible-light-driven photocatalysts. Int J Hydrogen Energy 42:25969–25979

[9] Huang R-L, Huang W-Q, Li D-F et al (2018) Self-assembled hierarchical carbon/g-C_3N_4 composite with high photocatalytic activity. J Phys D Appl Phys 51:135501

[10] Lou Z, Xue C (2016) In situ growth of WO_{3-x} nanowires on g-C_3N_4 nanosheets: 1D/2D heterostructures with enhanced photocatalytic activity. CrystEngComm 18:8406–8410

[11] Guo L, Yang Z, Marcus K et al (2018) MoS_2/TiO_2 heterostructures as nonmetal plasmonic photocatalysts for highly efficient hydrogen evolution. Energy Environ Sci 11:106–114

[12] Wang W, Fang J, Shao S, Lai M, Lu C (2017) Compact and uniform TiO_2@g-C_3N_4 core-shell quantum heterojunction for photocatalytic degradation of tetracycline antibiotics. Appl Catal B 217:57–64

[13] Chen D, Wang K, Ren T, Ding H, Zhu Y (2014) Synthesis and characterization of the ZnO/mpg-C_3N_4 heterojunction photocatalyst with enhanced visible light photoactivity. Dalton Trans 43:13105–13114

[14] Li M, Zhang L, Wu M et al (2016) Mesostructured CeO_2/g-C_3N_4 nanocomposites: Remarkably enhanced photocatalytic activity for CO_2 reduction by mutual component activations. Nano Energy 19:145–155

[15] Huang K, Hong Y, Yan X et al (2016) Hydrothermal synthesis of g-C_3N_4/$CdWO_4$ nanocomposite and enhanced photocatalytic activity for tetracycline degradation under visible light. CrystEngComm 18:6453–6463

[16] Qiao Q, Yang K, Ma L-L et al (2018) Facile in situ construction of mediator-free direct Z-scheme g-C_3N_4/CeO_2 heterojunctions with highly efficient photocatalytic activity. J Phys D Appl Phys 51:275302

[17] Yuan Y, Huang G-F, Hu W-Y et al (2017) Construction of g-C_3N_4/CeO_2/ZnO ternary photocatalysts with enhanced photocatalytic performance. J Phys Chem Solids 106:1–9

[18] Liang Q, Li Z, Bai Y, Huang Z-H, Kang F, Yang Q-H (2017) A composite polymeric carbon nitride with in situ formed isotype heterojunctions for highly improved photocatalysis under visible light. Small 13:1603182

[19] Hong J, Xia X, Wang Y, Xu R (2012) Mesoporous carbon nitride with in situ sulfur doping for enhanced photocatalytic hydrogen evolution from water under visible light. J Mater Chem 22:15006–15012

[20] Zhang J, Chen X, Takanabe K et al (2010) Synthesis of a carbon nitride structure for visible-light catalysis by copolymerization. Angew Chem Int Ed 49:441–444

[21] Dong F, Sun Y, Wu L, Fu M, Wu Z (2012) Facile transformation of low cost thiourea into nitrogen-rich graphitic carbon nitride nanocatalyst with high visible light photocatalytic performance. Catal Sci Technol 2:1332–1335

[22] Xu J, Wu H-T, Wang X et al (2013) A new and environmentally benign precursor for the synthesis of mesoporous g-C_3N_4 with tunable surface area. Phys Chem Chem Phys 15:4510–4517

[23] Lin Z, Wang X (2013) Nanostructure engineering and doping of conjugated carbon nitride semiconductors for hydrogen photosynthesis. Angew Chem Int Ed 52:1735–1738

[24] Zhang J, Zhang M, Sun R-Q, Wang X (2012) A facile band alignment of polymeric carbon nitride semiconductors to construct isotype heterojunctions. Angew Chem Int Edit 51:10145–10149

[25] Dong F, Zhao Z, Xiong T et al (2013) In situ construction of g-C_3N_4/g-C_3N_4 metal-free heterojunction for enhanced visible-light photocatalysis. ACS Appl Mater Int 5:11392–11401

[26] Dong F, Ni Z, Li P, Wu Z (2015) A general method for type I and type II g-C_3N_4/g-C_3N_4 metal-free isotype heterostructures with enhanced visible light photocatalysis. New J Chem 39:4737–4744

[27] Liu C, Dong X, Hao Y et al (2017) A novel supramolecular preorganization route for improving g-C_3N_4/g-C_3N_4 metal-free homojunction photocatalysis, New. J Chem 41:11872–11880

[28] Wasio NA, Quardokus RC, Forrest RP et al (2014) Self-assembly of hydrogen-bonded two-dimensional quasicrystals. Nature 507:86–89

[29] Whitesides GM, Mathias JP, Seto CT (1991) Molecular self-assembly and nanochemistry: a chemical strategy for the synthesis of nanostructures. Science 254:1312–1319

[30] Shalom M, Inal S, Fettkenhauer C, Neher D, Antonietti M (2013) Improving carbon nitride photocatalysis by supramolecular preorganization of monomers. J Am Chem Soc 135:7118–7121

[31] Jun Y-S, Lee EZ, Wang X et al (2013) From melamine–cyanuric acid supramolecular aggregates to carbon nitride hollow spheres. Adv Funct Mater 23:3661–3667

[32] Jun Y-S, Park J, Lee SU et al (2013) Three-dimensional macroscopic assemblies of low-dimensional carbon nitrides for enhanced hydrogen evolution. Angew Chem Int Edit 52:11083–11087

[33] Xu J, Wang H, Zhang C et al (2017) From millimeter to subnanometer: vapor–solid deposition of carbon nitride hierarchical nanostructures directed by supramolecular assembly. Angew Chem Int 56:8426–8430

[34] Li L, Zhao Y, Antonietti M, Shalom M (2016) New organic semiconducting scaffolds by supramolecular preorganization: dye intercalation and dye oxidation and reduction. Small 12:6090–6097

[35] Yang XL, Qian FF, Zou GJ et al (2016) Facile fabrication of acidified g-C_3N_4/g-C_3N_4 hybrids with enhanced photocatalysis performance under visible light irradiation. Appl Catal B 193:22–35

[36] Wang D, Xu Z, Luo Q et al (2016) Preparation and visible-light photocatalytic performances of g-C_3N_4 surface hybridized with a small amount of CdS nanoparticles. J Mater Sci 51:893–902

[37] Ishida Y, Chabanne L, Antonietti M, Shalom M (2014) Morphology control and photocatalysis enhancement by the one-pot synthesis of carbon nitride from preorganized hydrogen-bonded supramolecular precursors. Langmuir 30:447–451

[38] Niu P, Zhang L, Liu G, Cheng H-M (2012) Graphene-like carbon nitride nanosheets for improved photocatalytic activities. Adv Funct Mater 22:4763–4770

[39] Yang X, Qian F, Zou G et al (2016) Facile fabrication of acidified g-C_3N_4/g-C_3N_4 hybrids with enhanced photocatalysis performance under visible light irradiation. Appl Catal B 193:22–35

[40] Lu X, Xu K, Chen P, Jia K, Liu S, Wu C (2014) Facile one step method realizing scalable production of g-C_3N_4 nanosheets and study of their photocatalytic H_{-2} evolution activity. J Mater Chem A 2:18924–18928

[41] Shi L, Li Z, Marcus K et al (2018) Integration of Au nanoparticles with a g-C_3N_4 based heterostructure: switching charge transfer from type-II to Z-scheme for enhanced visible light photocatalysis. Chem Commun 54:3747–3750